

Biochemical and structural studies of two tetrameric nucleoside 2'-deoxyribosyltransferases from psychrophilic and mesophilic bacteria: Insights into cold-adaptation

Jesús Fernández-Lucas, Iván Acebrón, Ruiying Wu, Yohana Alfaro, Javier Acosta, Pierre-Alexandre Kaminski, Miguel Arroyo, Andrzej Joachimiak, Boguslaw Nocek, Isabel de La Mata, et al.

▶ **To cite this version:**

Jesús Fernández-Lucas, Iván Acebrón, Ruiying Wu, Yohana Alfaro, Javier Acosta, et al.. Biochemical and structural studies of two tetrameric nucleoside 2'-deoxyribosyltransferases from psychrophilic and mesophilic bacteria: Insights into cold-adaptation. International Journal of Biological Macromolecules, 2021, 192, pp.138-150. 10.1016/j.ijbiomac.2021.09.164 . pasteur-03549990

HAL Id: pasteur-03549990

https://pasteur.hal.science/pasteur-03549990

Submitted on 31 Jan 2022

HAL is a multi-disciplinary open access archive for the deposit and dissemination of scientific research documents, whether they are published or not. The documents may come from teaching and research institutions in France or abroad, or from public or private research centers.

L'archive ouverte pluridisciplinaire **HAL**, est destinée au dépôt et à la diffusion de documents scientifiques de niveau recherche, publiés ou non, émanant des établissements d'enseignement et de recherche français ou étrangers, des laboratoires publics ou privés.



Distributed under a Creative Commons Attribution - NonCommercial - NoDerivatives 4.0 International License

International Journal of Biological Macromolecules 192 (2021) 138–150

Contents lists available at ScienceDirect

International Journal of Biological Macromolecules

journal homepage: www.elsevier.com/locate/ijbiomac

Biochemical and structural studies of two tetrameric nucleoside 2′-deoxyribosyltransferases from psychrophilic and mesophilic bacteria: Insights into cold-adaptation

Jesús Fernández-Lucas [a,b], Iván Acebrón [c], Ruiying Y. Wu [d], Yohana Alfaro [e], Javier Acosta [a], Pierre A. Kaminski [f], Miguel Arroyo [e], Andrzej Joachimiak [c,g,h], Boguslaw P. Nocek [d], Isabel De la Mata [e], José M. Mancheño [c,*]

[a] Applied Biotechnology Group, Universidad Europea de Madrid, Urbanización El Bosque, E-28670 Villaviciosa de Odón, Madrid, Spain
[b] Grupo de Investigación en Ciencias Naturales y Exactas, GICNEX, Universidad de la Costa, CUC, Calle 58 # 55 66, Barranquilla, Colombia
[c] Department of Crystallography and Structural Biology, Institute Rocasolano (CSIC), Serrano 119, 28006 Madrid, Spain
[d] Bioscience Division, Argonne National Laboratory, Argonne, IL 60439, USA
[e] Department of Biochemistry and Molecular Biology I, Faculty of Biology, Complutense University of Madrid, C/José Antonio Nováis 2, 28040 Madrid, Spain
[f] Institut Pasteur, Unité Biologie des Bactéries Pathogènes à Gram-positif, CNRS URL3526, Paris, France
[g] Structural Biology Center, X-ray Science Division, Argonne National Laboratory, Argonne, IL 60439, USA
[h] Department of Biochemistry and Molecular Biology, The University of Chicago, Chicago, IL 60367, USA

ARTICLE INFO

Keywords:
2′-Deoxyribosyltransferases
Crystal structure
Psychrophilic enzymes

ABSTRACT

Nucleoside 2′-deoxyribosyltransferases (NDTs) catalyze the cleavage of glycosidic bonds of 2′-deoxynucleosides and the following transfer of the 2′-deoxyribose moiety to acceptor nucleobases. Here, we report the crystal structures and biochemical properties of the first tetrameric NDTs: the type I NDT from the mesophilic bacterium *Enterococcus faecalis* V583 (*Ef*PDT) and the type II NDT from the bacterium *Desulfotalea psychrophila* (*Dp*NDT), the first psychrophilic NDT. This novel structural and biochemical data permitted an exhaustive comparative analysis aimed to shed light into the basis of the high global stability of the psychrophilic *Dp*NDT, which has a higher melting temperature than *Ef*PDT (58.5 °C *versus* 54.4 °C) or other mesophilic NDTs. *Dp*NDT possesses a combination of unusual structural motifs not present neither in *Ef*PDT nor any other NDT that most probably contribute to its global stability, in particular, a large aliphatic isoleucine-leucine-valine (ILV) bundle accompanied by a vicinal disulfide bridge and also an intersubunit disulfide bridge, the first described for an NDT. The functional and structural features of *Dp*NDT do not fit the standard features of psychrophilic enzymes, which lead us to consider the implication of (sub)cellular levels together with the protein level in the adaptation of enzymatic activity to low temperatures.

1. Introduction

Nucleoside 2′-deoxyribosyltransferases (EC: 2.4.2.6) catalyze the transglycosylation reaction of the 2′-deoxyribose moiety between purine and/or pyrimidine bases [1,2]. These enzymes were initially discovered in *Lactobacilli*, which evolved salvage pathways to scavenge exogenous deoxynucleosides to synthesize their DNA [3]. In these bacteria, NDTs play a similar role to nucleoside phosphorylases [4]. However, NDTs are not exclusive from *Lactobacilli* and are also present in other bacteria such as *Streptococcus* [5], the parasitic *Borrelia burgdorferi* [6], the psychrotolerant *Bacillus psychrosaccharolyticus* [7], the extremophile cyanobacterium *Chroococcidiopsis thermalis* [8], and also in parasitic unicellular eukaryotic organisms such as *Crithidia luciliae* [9], *Leishmania mexicana* [10], and *Trypanosoma brucei* [11]. Currently, various structures of NDTs have been reported from bacterial sources: *Lactobacillus leichmannii* (*Ll*NDT) [12], *Lactobacillus helveticus* (*Lh*PDT) [13] and *Bacillus psychrosaccharolyticus* (*Bp*NDT) [7], and also from the eukaryotes *Leishmania mexicana* (*Lm*PDT) [10] and *Trypanosoma brucei* (*Tb*PDT) [11]. Whereas bacterial NDTs are homohexamers endowed with dihedral D3 molecular symmetry [10], eukaryotic NDTs are homodimers [10]. The basic catalytic unit [12] of all these enzymes is a dimeric assembly where each active site is configured by residues contributed by

* Corresponding author.
E-mail address: xjosemi@iqfr.csic.es (J.M. Mancheño).

https://doi.org/10.1016/j.ijbiomac.2021.09.164
Received 19 May 2021; Received in revised form 22 September 2021; Accepted 24 September 2021
Available online 5 October 2021
0141-8130/© 2021 The Author(s). Published by Elsevier B.V. This is an open access article under the CC BY-NC-ND license (http://creativecommons.org/licenses/by-nc-nd/4.0/).

both polypeptide chains that despite sharing a low level of sequence identity between them their 3D structure is highly conserved. In fact, we reported only minor changes between the architectures of the subunits from dimeric and hexameric NDTs [10]. With the exception of *Bp*NDT, which is produced by the psychrotolerant bacterium *B. psychrosaccharolyticus*, the other NDTs with known 3D structure described up to now are mesophilic enzymes. In this regard, we found that *Bp*NDT behaves as a mesophilic enzyme with an optimal temperature for activity of 50 °C [7], well above the maximum temperature for bacterial growth (30 °C). Shorter, flexible loops around the active site of *Bp*NDT than in *Lh*PDT and *Ll*NDT suggested a mechanism of adaptation to low temperatures [7]; however, all these NDTs are characterized by an irregular region situated at the entrance of the active site which is highly flexible and usually poorly defined [7,10–13]. This makes the relation of flexibility with stability very difficult to define in NDTs, as suggested before for other cases [14].

To shed light into the structural basis of the adaptation to cold conditions of NDTs, in this work we determined the crystal structures of *Dp*NDT, a type II 2′-deoxyribosyltransferase from the psychrophilic bacterium *Desulfotalea psychrophila*, and also *Ef*PDT, a type I 2′-deoxyribosyltransferase from the mesophilic bacterium *Enterococcus faecalis* V583. Since both enzymes are tetramers, which is a novel oligomeric state within the NDT family, their exhaustive comparative analysis can be made from a more solid perspective. We found within the structure of *Dp*NDT unusual structural motifs that may contribute to its high global stability when compared to *Ef*PDT and other mesophilic, dimeric and hexameric NDTs.

2. Materials and methods

2.1. Chemicals

Cell culture media reagents were from Difco (San Louis, Mo, USA). Enzyme substrates and chemical reagents were from Sigma-Aldrich. Natural and non-natural bases were purchased Carbosynth Ltd. (Compton, United Kingdom), except arabinosyl nucleosides which were a gift from Bio Sint (Italy) and 2′-fluoro-2′-deoxyribonucleosides which were supplied by Rasayan Inc. (California, USA).

2.2. Cloning of the dpndt and efpdt genes

The *dpndt* gene encoding a putative NDT from *Desulfotalea psychrophila* DSM 12343 was amplified by PCR using the chromosomal DNA from this microorganism as template, previously prepared with the DNeasy kit (Qiagen). The PCR primers used were: Q6AQBO*Nco*I (5′-CATGCCATGGATAATTTATCGTTCAGACCAAAATTGTACC-3′) and Q6AQBO*Hind*III (5′-AAAAGCTTTTAGCTGAGTTTATTATATTTTTGCTGTAACC-3′). The restriction sites *Nco*I and *Hind*III (underlined) were included to facilitate subcloning. The amplified 0.5 kb product was subcloned following standard procedures into the pET24d(+) vector and the resultant plasmid, pET24-*Dp*NDT was used to transform competent *E. coli* DH5α cells. After confirming the correctness of the *Dpndt* sequence, this vector was then used to transform *E. coli* BL21(DE3) cells for protein overproduction.

As a result of the cloning strategy the final sequence of the recombinant *Dp*NDT protein herein studied differs from the original one (UniprotKB: Q6AQB0) in that it lacks the first five amino acid residues and Asn7 is replaced with Asp7. Numbering of the *Dp*NDT sequence used in this work refers to the complete sequence.

The *efpdt* gene construct for *Ef*PDT used in crystallization assays was amplified from genomic DNA from *Enterococcus faecalis* V583. The PCR primers for the construct were 5′-TACTTCCAATCCAATGCCATGACAAAAATTTATTTTGCAGGACCTTTATTTTCG-3′ forward and 5′-TTATCCACTTCCAATGTTATGACAATCGTTGCTTAATTTCTTCCAACA AATC-3′reverse. The purified PCR product was cloned into the expression vector pMCSG7 using a modified LIC protocol as described earlier [15]. Conversely, the *efpdt* gene coding for *Ef*PDT used for biochemical analyses (NCBI Reference Sequence: WP_002359788.1), and the *hisdpndt* and *hisdpndtc92s* genes coding for N-terminal his-tagged wild-type *Dp*NDT (His-*Dp*NDT) and Cys92Ser *Dp*NDT (His-*Dp*NDTC92S), respectively, were purchased from Genscript® (Piscataway, United States). The coding sequences were subcloned as *Nde*I-*Bam*HI fragment for *efpdt* into the expression vectors pET28b(+), and as *NdeI-XhoI* fragment for *hisdpndt* and *hisdpndtc92s* into the expression vector pET28a(+). The resulting recombinant vectors were pET28b*Ef*PDT, pET28aHis*Dp*NDT and pET28aHis*Dp*NDTC92S, respectively.

2.3. Overproduction and purification of recombinant enzymes

Recombinant *Dp*NDT was produced as follows: *E. coli* BL21(DE3) cells harbouring the pET24*Dp*NDT vector were grown at 37 °C in LB liquid medium supplemented with kanamycin (50 μg/mL). When cultures reached an optical density of 0.8 at 600 nm, *dpndt* expression was induced with 0.4 mM IPTG for 2.5 h. Then, cells were harvested by centrifugation at 3500×*g* for 15 min., resuspended in 10 mM potassium phosphate buffer pH 7 (buffer A) and broken by ultrasonic treatment using a Branson Digital Sonifier (USA). The cell-free extract was applied onto a 5 mL Econo-Pac® High Q cartridge (Bio-Rad, USA) equilibrated in the same buffer. The column was extensively washed with buffer A and then the protein was eluted with a linear gradient of 0-0.4 M NaCl in buffer A. Fractions containing *Dp*NDT were pooled and concentrated with polyethylenglycol 35,000 (Sigma, USA) (reverse dialysis) and loaded onto a Superose 12 Fast Flow column (Amersham Biosciences, UK) equilibrated in 50 mM potassium phosphate buffer, pH 7.0 (buffer B). Purity of the *Dp*NDT sample was checked by SDS-PAGE. Protein concentration was determined according to Bradford [16]. N-terminal sequence of *Dp*NDT was determined by Edman degradation methodology.

SeMet-labeled EfPDT production and purification was as follows: the EfPDT expression vector was transformed into E.coli BL21 (DE3) and EfPDT was produced as an N-terminal His_6-tagged protein. The starter culture was grown at 32 °C overnight in modified M9 media as described [17]. Once the 1 L culture reached OD_{600} ~ 1.4 and cool down to 18 °C, inhibitory amino acids (25 mg each of L-valine, L-isoleucine, L-leucine, L-lysine, L-threonine, L-phenylalanine) and 60 mg selenomethionine (Medicillin, Inc., for SeMet-labeled protein only) were added. After induction with 0.5 mM IPTG, cells were incubated overnight at 18 °C, harvested by centrifugation and the cell pellet re-suspended in 30 mL of lysis buffer (50 mM HEPES pH 8.0, 500 mM NaCl, 5% (v/v) glycerol, 10 mM imidazole, 10 mM β-mercaptoethanol, and 1 protease inhibitor cocktail tablet (Complete, Roche)) and stored at -80 °C before processing.

Cell lysates were centrifuged and filtered and applied onto a 5 mL HiTrap Ni-NTA column (GE Healthcare Life Sciences) with an ÄKTAxpress system (GE Healthcare Life Sciences). After washing, the His_6-tagged protein was eluted with elution buffer (500 mM NaCl, 5% glycerol, 50 mM HEPES pH 8.0, 250 mM imidazole, and 10 mM 2-mercaptoethanol) and the fusion tag was removed by treatment with recombinant His_7-tagged TEV protease. Subtractive Ni-NTA affinity chromatography was used to remove the His_6-tag, uncut protein, and His_7-tagged TEV protease. Purified *Ef*PDT was dialyzed against crystallization buffer (150 mM NaCl, 20 mM HEPES pH 8.0, and 1 mM DTT) and then concentrated to 35 mg/mL, flash-cooled, and stored in liquid nitrogen until used for crystallization.

*Ef*PDT for biochemical analyses and N-terminal His-tagged *Dp*NDT and *Dp*NDTC92S were produced and purified as described before [8]. Briefly, *Ef*PDT, His-*Dp*NDT and His-*Dp*NDTC92S were produced in *E. coli* BL21(DE3) cells containing the expression vectors pET28b*Ef*PDT, pET28aHis*Dp*NDT and pET28aHis*Dp*NDTC92S respectively, grown at 37 °C in LB medium containing kanamycin 50 μg/mL. Protein production was induced by adding 0.5 mM IPTG and the cells were further grown for 3 h. Cells were harvested by centrifugation at 3500 ×*g* and the

resulting pellet was resuspended in 10 mM sodium phosphate buffer pH 7. Crude extracts were prepared by French press lysis of cell suspensions. The lysate was centrifuged at 17,500×*g* for 30 min and the supernatant was filtered through a 0.22-μm filter (Millipore). The cleared lysate was loaded onto a 5 mL HisTrap FF column (GE Healthcare) pre-equilibrated in a binding buffer (20 mM Tris-HCl buffer, pH 8.0, with 100 mM NaCl and 10 mM imidazole) and the column was washed. Bound proteins were eluted using a linear gradient of imidazole (from 10 to 500 mM). Fractions containing *Ef*PDT, His-*Dp*NDT or His-*Dp*NDTC92S were identified by SDS-PAGE, pooled, concentrated, and loaded onto a HiLoad 16/60 Superdex 200 prep grade column (GE Healthcare) pre-equilibrated in 50 mM sodium phosphate, pH 7.0. Fractions with the protein of interest identified by SDS-PAGE were pooled, and the protein was dialyzed against 10 mM sodium phosphate, pH 7.0, and concentrated and stored at 4 °C until its use.

2.4. N-deoxyribosyltransferase assays

The standard *N*-deoxyribosyltransferase activity assays were as follows: for *Dp*NDT, 5 μL of cell-free extract or 14.3 μg of pure enzyme were incubated with a solution of 2′-deoxyuridine and thymine (10 mM final concentration in 50 mM MES buffer pH 6.5; final volume of 40 μL) for 10 min at 40 °C; for *Ef*PDT, 5.375 μg of pure His-tagged enzyme was incubated with a 40 μL solution containing 1 mM 2′-deoxyinosine (dIno), 1 mM adenine (Ade) in 50 mM phosphate buffer, pH 7.0 for 5-10 min at 40 °C (300 rpm). The reactions were stopped by addition of 40 μL of cold methanol in ice-bath and heated at 95 °C for 5 min. After centrifugation of the samples at 9000×*g* for 2 min, 50 μL of each supernatant were diluted with 50 μL of water and the production of nucleosides was analyzed by HPLC (Agilent 1100 series) with a LUNA C-18 (2) column (dimensions: 250 × 46 mm; particle size: 5 μ; Phenomenex, USA). The elution conditions were: 0-10 min, 100-90% trimethyl ammonium acetate and 0-10% acetonitrile, and 10-20 min, 90-100% trimethyl ammonium acetate and 10-0% acetonitrile. The flow rate was fixed at 1 mL/min and the pressure was 180 bar. Four wavelengths were used for detection 254, 260, 240 and 230 nm. One unit of enzyme activity was defined as the amount of enzyme required to produce 1 μmol of product per minute under standard conditions.

Enzymatic synthesis of natural nucleosides was performed as described for the NDT standard assay using different 2′-deoxyribonucleosides and bases (10 mM) and the enzymatic synthesis of non-natural nucleosides was carried out from natural or non-natural deoxyribonucleosides and bases at different conditions. The production of nucleosides was detected by HPLC as described above. All measurements were carried out in triplicate. Retention times for the different bases were those described previously [18]. Their names are here abbreviated according to the recommendations of the IUPAC-IUB Commission on Biochemical Nomenclature.

2.5. Biochemical characterization

Dependence of *Dp*NDT activity on pH was determined by measuring its activity in standard conditions using 10 mM potassium citrate-phosphate-borate buffer at different pH values (4.0 to 10.5), with a constant ionic strength, adjusted by addition of NaCl. Conversely, dependence of *Dp*NDT stability on pH was studied by incubating 14.3 μg of pure recombinant enzyme in 10 mM potassium citrate-phosphate-borate buffer at different pH values (from 4.0 to 12.0) for 15 min at 4 °C. Remaining *Dp*NDT activity was then measured in the standard conditions after adjusting the pH of the samples to 6.5 by addition of 50 mM MES buffer. Ionic strength of all samples was maintained constant (150 mM) by addition of NaCl. Buffers sodium citrate (pH 3.0-6.0), sodium phosphate (pH 6.0-8.0), and sodium borate (pH 8.0-10.0) were used as reaction buffers (50 mM) for *Ef*PDT activity assays as previously described [17,19].

DpNDT activity was measured at different temperatures (from 20 to 80 °C) under standard conditions. Thermal inactivation kinetics of DpNDT was studied by incubating the enzyme (14.3 μg) for different times at 40 °C, 50 °C and 60 °C in 50 mM MES buffer, pH 6.5. At regular time intervals, 5 μL aliquots were withdrawn from the incubation mixtures and the residual activity was determined under the standard assay conditions. The experimental data were modeled as described previously [18] to determine thermal inactivation constants and DpNDT lifetimes at the three temperatures analyzed. Thermal inactivation kinetics of His-DpNDT and His-DpNDTC92S were carried out at 50 °C up to 24 h. incubation. For EfPDT, the optimum temperature was determined using the standard assay across 20-80 °C range.

2.6. Analytical ultracentrifugation analysis

Sedimentation velocity and equilibrium experiments of *Dp*NDT were carried out at different protein concentrations (1 mg/mL, 0.5 mg/mL y 0.25 mg/mL) in 50 mM potassium phosphate buffer pH 7, at 20 °C and 50,000 × *g* in an Optima XL-I analytical ultracentrifuge (Beckman-Coulter Inc.), equipped with absorbance optics, using an An-60Ti rotor and standard (12 mm optical path) double-sector centre pieces of Epon-charcoal. Baseline offsets were determined at 200,000 × *g*. The apparent sedimentation coefficient distribution *c(s)*, and sedimentation coefficient *s* were calculated from the sedimentation velocity data using the program SEDFIT [20] and the whole-cell weight-average bM_w (buoyant molar mass) values were estimated by fitting the experimental data to the equation for the radial concentration distribution of an ideal solute at sedimentation equilibrium using the program EQASSOC supplied by Beckman-Coulter [21]. The corresponding apparent weight-average molar masses (M_w) were determined from the buoyant masses, considering the partial specific volumes obtained from the amino acid composition of *Dp*NDT with the program SEDNTERP [22].

2.7. Far-UV CD spectroscopy

Far-UV CD measurements were carried out on a Jasco J-810 spectropolarimeter (Jasco Inc., Easton, MD, USA) equipped with a thermostated cell holder and a Peltier temperature control accessory. Thermal transitions of *Ef*PDT, *Dp*NDT, His-*Dp*NDT and His-*Dp*NDTC92S were recorded in 0.1-cm path length quartz cell cuvettes using a protein concentration of 0.3 mg/ mL (20 mM sodium phosphate buffer, pH 7.0) by monitoring the variation of the ellipticity at 220 nm as the temperature was increased from 25 to 80 °C at 60 °C h^{-1}. CD scans were recorded from 250 to 200 nm, (bandwidth, 1 nm; response, 2 s; scan speed, 50 nm min^{-1}). Baseline subtraction was performed in all cases. Results are expressed as mean residue ellipticity [ϕ]MRW, in units of degree cm^2 $dmol^{-1}$ of amino acid (Mr = 110 for this protein). The normalized ellipticity value at each temperature was calculated as $([\phi]_T - [\phi]_{25})/([\phi]_{80} - [\phi]_{25})$, where $[\phi]_T$ is the ellipticity value at temperature T, and $[\phi]_{25}$ and $[\phi]_{90}$ are the ellipticity values at 25 °C and 80 °C, respectively. Three different samples were analyzed. T_m values were estimated with the Calfitter web server [23]

2.8. Enzyme crystallization

*Ef*PDT was crystallized using sitting drop vapor diffusion at 297 K in a CrystalQuick® 96-well round-bottomed plate (Greiner Bio-One North America). Protein solution (400 nL) was mixed with 400 nL of crystallization reagent using the Mosquito® nanoliter liquid workstation (TTP LabTech) and allowed to equilibrate against 140 μL of crystallization reagent. The plate was then incubated at 291 K. Four different crystallization screens were used: Index and PEG-ion (Hampton), Wizard I and Wizard II (Rigaku). The best crystals of *Ef*PDT were obtained in PEG-ion condition 20 consisting of 20% PEG 3350, 0.2 M Magnesium Formate, pH 5.9. Conversely, crystallization of *Dp*NDT was performed at 291 K by the sitting-drop vapor diffusion method with Innovaplate SD-2 96-well plates and a Nanodrop Innovadyne robot. Each drop contained 250 nL

of protein (*Dp*NDT: 10 mg/mL) in Tris–HCl buffer (20 mM Tris–HCl pH 8.0 containing 0.1 M NaCl) and 250 nL of reservoir solution. Drops were equilibrated against 65 μL reservoir solution. High-quality diffraction crystals were observed in several PEG-containing conditions. The crystallization conditions of the best diffracting crystals were: 20% PEG 3350, 0.1 M sodium malonate for *Dp*NDT.

2.9. X-ray diffraction and structure determination

For diffraction data collection, the crystals were transferred to a cryoprotectant solution consisting of mother liquor plus glycerol 10–15% (v/v) for EfPDT and 20% (v:v) for DpNDT, before being cooled to 100 K in a cold nitrogen-gas stream. Diffraction data from the EfPDT crystal were collected at the 19-ID beamline of the Structural Biology Center at the Advanced Photon Source, Argonne National Laboratory for EfPDT. Single-wavelength anomalous dispersion (SAD) data at 0.9794 Å (12.6605 keV) near the absorption peak for selenium were collected from a single SeMet-labeled EfPDT crystal. The absorption peak energy was determined using the X-ray fluorescence scan. All the EfPDT data were collected using SBCCOLLECT and processed and scaled by the HKL3000 suite [24]. Equally, diffraction data from DpNDT crystals were collected at beamline ID29 at the European Synchrotron Radiation Facility (ESRF) (Grenoble, France). Images were processed with XDS [25] and the space group examination was performed with POINTLESS [26].

The structure of EfPDT was determined by SAD phasing using HKL3000 [24] with the following steps: the 4 selenium (Se) sites were located by SHELXC and SHELXD [27], the handedness of the substructure Se sites was checked by SHELXE [27], phasing was done by MLPHARE [28], density modification was done as published [29]. The initial model was built from SHELXE [27] and then completed manually using COOT [30]. In turn, the structure of DpNDT was solved by molecular replacement with phenix.phaser [31], using the atomic coordinates of EfPDT as search model. Model rebuilding was performed manually using COOT [30] and refinement was carried out with REFMAC [32] for EfPDT and phenix.refine [33] in PHENIX [34] for DpNDT. In the EfPDT structure, there was no interpretable electron density for residues 44-45 and residue 159 at the C-terminal end of chain B and residue 159 at the C-terminal end of chain A. Main chain torsion angles of all residues of the structure fell within acceptable regions of Ramachandran plots. The definitive refined structures have a final R-factor of 22.0% (R_{free} = 27.7%) for DpNDT and 17.5% (R_{free} = 21.7%) for EfPDT. Analysis of the interfacial surfaces was done with the PISA server [35] and secondary structure assignment was done with DSSP [36]. Stereochemistry validation was done with the MolProbity tool plus from wwPDB Deposition server. PyMOL [37] was used for structure visualization and figure preparation. Data collection and refinement statistics are listed in Table 1.

Table 1
Data collection and refinement statistics.

	*Ef*PDT	*Dp*NDT
PDB code	7M5H	7O62
Data collection		
Synchrotron source	APS	ESRF
Beamline	19ID	ID29
Wavelength (Å)	0.9794	0.9792
Space group	$F4_132$	$P2_12_12_1$
Unit-cell parameters	$a = b = c =$ 219.90 $\alpha = \beta = \gamma = 90°$	$a = 55.17$; $b = 86.37$; $c =$ 140.93 $\alpha = \beta = \gamma = 90°$
Resolution range (Å)	2.15-40 (2.15-2.19)	2.40-46.98 (2.4-2.53)
No. of measured reflections[a]	293,619(14346)	357,582 (49,715)
No. of unique reflections	25,312(1238)	27,119 (3856)
Mean ($I/\sigma I$)	33.64 (3.1)	14.8 (3.2)
Completeness (%)	99.9 (99.9)	99.9 (99.9)
Multiplicity	11.6 (11.6)	13.2 (12.9)
B-factor (Wilson plot, Å^2)	35.97	42.1
R_{meas} (%); R_{pim} (%)	7.9 (76.4); –	10.4 (73.7); 2.9 (20.4)
Refinement		
Reflections used in refinement	25,244	26,665
Reflections used for R_{free}	1291	1342
Protein	2/2464	4/4171
Others	2/12	4/24
Water	244/244	20/20
R_{work}(%)/R_{free}(%)	17.5/21.7	20.3/26.1
Rms deviation bond length (Å)	0.001	0.012
Rms deviation angles (°)	0.417	1.064
Ramachandran		
Favoured (%)	98.72	93.8
Allowed (%)	1.28	4.7

[a] Values for the highest resolution shell are given in parentheses.

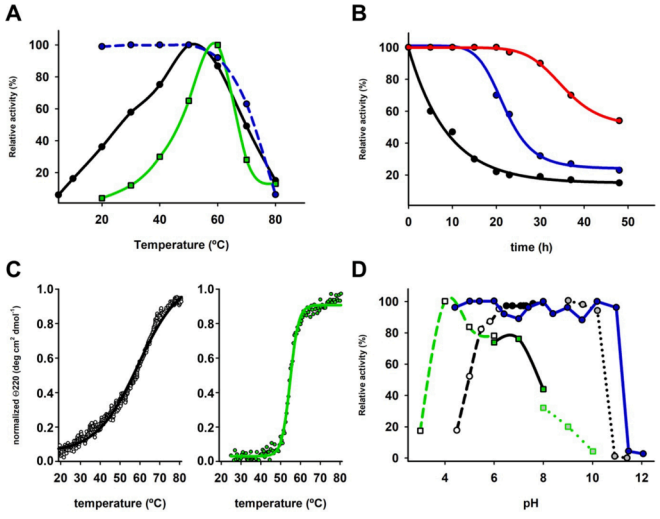


Fig. 1. Biochemical characterization of *Ef*PDT and *Dp*NDT. (a) Effect of temperature on *Ef*PDT (*green*) and *Dp*NDT (*black*) activities, and on *Dp*NDT stability (*blue*). (b) Thermal deactivation profile of *Dp*NDT at 40 °C (*red*), 50 °C (*blue*) and 60 °C (black). (c) Thermal unfolding of *Ef*PDT (*green*) and of *Dp*NDT followed by far-UV CD (*black*). (d) pH dependence of *Ef*PDT (*green lines or symbols*) *Dp*NDT (*black dashed or dotted lines*) activities, and *Dp*NDT stability at different pH values (*blue lines*).

3. Results and discussion

3.1. Biochemical characterization of recombinant DpNDT and EfPDT

The genus *Desulfotalea* comprises obligately or facultatively psychrophilic, Gram negative bacteria, with optimal temperatures for growth within the range 10-18 °C [38]. In particular, the temperature range for growth of *D. psychrophila* is between -1.8 and 19 °C, with an optimal growth temperature at 10 °C. Unexpectedly, we observed very low 2′-deoxyribosyltransferase activity for *Dp*NDT in the temperature range of 10-15 °C using standard assay conditions (Fig. 1A) that were deduced from studying diverse combinations of acceptors and donors at higher temperatures (Table 2). *Dp*NDT activity increased as the temperature was raised (see below), up to values well above the reported temperature range for growth of this bacterium. To provide insights into this apparently paradoxical enzyme [39] with very low *in vitro* activity at optimal bacterial growth temperature and high activity at "biologically forbidden" temperatures, we analyzed its main biochemical and structural characteristics and compared them with those from the mesophilic closest structural homolog *Ef*PDT. This latter enzyme is ′roduced by the Gram positive, commensal bacterium *Enterococcus faecalis* V583 that inhabits the gastrointestinal tracts of healthy human and other mammals, although it can cause life-threatening, nosocomial infections. In this case, as expected, high activity is observed within the

Table 2
Transferase activity of *Ef*PDT and *Dp*NDT.

*Ef*PDT specific activity (IU/mg)[a,b]				*Dp*NDT specific activity (IU/mg)[c]					
	dAdo	dGuo	dIno		dAdo	dCyd	dIno	dThd	dUrd
Ade	–	0.07	0.13	Ade	–	0.02	0.11	0.21	0.14
Gua	0.13	–	0.10	Cyt	0.02	–	0.04	0.04	0.06
Hyp	0.08	0.05	–	Hyp	0.02	0.01	–	0.72	0.67
				Thy	0.02	0.01	0.10	–	0.70
				Ura	0.07	0.02	0.11	0.73	–

[a] Reaction conditions: 5.375 μg of *Ef*PDT in 40 μL at 50 °C for 10 min, with 1 mM substrates in 50 mM MES buffer, pH 6.5 in a final volume of 40 μL
[b] Standard deviation values <0.005 in all cases.
[c] 14.3 μg of *Dp*NDT in 40 μL at 50 °C for 20 min, with 10 mM substrates in 50 mM MES buffer, pH 6.5 in a final volume of 40 μL.

temperature interval of bacterial growth (see below), up to temperature values where protein thermal unfolding occurs.

The transferase activity of DpNDT was studied against combinations of different natural ribo- or 2-deoxyribonucleosides as donors with various acceptor bases in different experimental conditions (Table 2). Whereas no activity was detected using ribonucleosides (not shown), 2′-deoxyribosyltransferase activity was detected when the donors dUrd or dThd were combined with the acceptors Thy and Hyp, or with the purine bases Ura or Hyp, respectively; no transferase activity was registered for dAdo as donor and just a modest one with dIno. This profile of activity suggests that the substituent at position C4 in pyrimidines (O atom in Thy and Ura versus amine group in Cyt) and at positions C2 in purines (no substituent in Ade and Hyp versus amine group in Gua) play important roles in productive binding to the enzyme. Whereas a marked preference for dUrd as donor has been described previously for other 2′-deoxyribosyltransferases [3,18,40,41], as far as we know lack of activity with Cyt as acceptor has not been reported previously. Taking these results into account we defined standard assay conditions for DpNDT as follows: donor, dUrd; acceptor, Thy; 10 mM final concentration in 50 mM MES buffer pH 6.5; final volume of 40 μL; for 10 min at 40 °C (see Materials and methods).

Using a similar approach, we showed that EfPDT specifically acts on purine 2′-deoxyribonucleosides, and that neither pyrimidine 2′-deoxynucleosides nor ribonucleosides are recognized (Table 2). Hence, since EfPDT exclusively recognizes purine 2′-deoxyribonucleosides must be classified as a type I NDT (PDT) and similarly, DpNDT as a type II NDT [2,10,13,18,42] since recognizes both purine and pyrimidine 2′-deoxyribonucleosides. When compared to other PDTs, EfPDT display activity values (0.13 IU/mg_{enz} in dAdo synthesis from dIno and Ade) in consonance with hexameric PDTs (LhPDT: 0.080 IU/mg_{enz} [3]; BpPDT: 0.080 IU/mg_{enz} [6]), but in stark contrast with the much higher active dimeric PDTs (TbPDT: 38.5 IU/mg_{enz}; LmPDT: 73.1 IU/mg_{enz}) [10,42]. Conversely, DpNDT can be considered as a poor catalyst, with activity values for dUrd synthesis from dThd and Ura (0.73 IU/mg_{enz}) much lower than those reported for other NDTs (Supplementary Table 1). The N-terminal, His-tagged DpNDT variants showed comparable activity values (His-DpNDT: 0.84 IU/mg_{enz}; His-DpNDTC92S: 0.91 IU/mg_{enz}). Nevertheless, this comparison can only be made in qualitative terms since experimental conditions of these latter activity assays are not identical to those reported here and can only be considered as an indirect reference for the DpNDT activity.

Thermal stability assays indicated that DpNDT activity remained stable up to a preincubation temperature of 50 °C (Fig. 1A), decreasing at ′igher values. Conversely, the effect of temperature on transferase activity indicated maximum activity around 50 °C, with residual activity at 10 °C (Fig. 1A). Similar thermal behaviour has been observed for two other enzymes from *D. psychrophila*: isocitrate dehydrogenase (DpIDH) [43,44], and o-succinyl-benzoate synthase [45], where enzymatic activity is observed well above the maximum growth temperature of the bacterium. High global stability of psychrophilic enzymes has been described elsewhere [46–48], and this apparent conflict with their a priori intrinsic thermal lability has been rationalized in terms of modulation of protein flexibility, mainly affecting active site regions to optimize the catalytic activity in cold conditions [49–51]. In contrast to these results, those from EfPDT are typical of a mesophilic enzyme, showing maximum activity in the 55-60 °C temperature range (Fig. 1A).

In order to differentiate between local effects on the active site of *Dp*NDT and global, structural effects of temperature, we analyzed the time dependent heat inactivation of the enzyme at three temperatures (40, 50 and 60 °C) (Fig. 1B and Supplementary Table 2), as well as its global thermal unfolding by far-UV CD (Fig. 1C). *Dp*NDT was inactivated at 40 and 50 °C following a first-order kinetics with a temperature-dependent lag period [52], and at 60 °C without such lag period. Analyses of the three data sets as described before [18], provided half-life values at the three temperatures studied of 48.5 h (at 40 °C), 21.4 h (at 50 °C) and 10.8 h (at 60 °C). Half-life values at 60 °C have been reported for the 2′-deoxyribonucleoside transferase from the mesophilic *Lr*NDT (17 min.) [18] and the psychrotolerant *Bp*NDT (21.8 h) [7], respectively. Hence, *Dp*NDT exhibits a half-life at 60 °C 2-fold lower to that of *Bp*NDT but 38-fold higher than that of *Lr*NDT, which is remarkable for an enzyme from a psychrophilic bacterium. Notably, this latter behaviour closely parallels the one observed between *Dp*IDH and its mesophilic homolog IDH from *Desulfitobacterium hafniense* [43].

A similar trend of high thermal stability was observed when analysing the melting temperature (T_m) of *Dp*NDT. The T_m value measured spectroscopically by far-UV CD (Fig. 1C) was 58.5 ± 0.5 °C, which is higher than the T_m of *Bp*NDT (55 °C) [7] but lower than the T_m for *Lr*NDT (64 °C) [18]. Since these latter results show the same trend as the ones observed for the heat-induced inactivation of *Dp*NDT it can be deduced that its temperature-induced loss of activity parallels the global unfolding of the enzyme and therefore cannot be ascribed to a specific heat-labile region. On the other hand, the thermal unfolding of *Ef*PDT studied by far-UV CD provides a T_m value of 54.4 ± 0.2 °C (Fig. 1C), which agrees with the temperature dependence of its transferase activity (Fig. 1A).

*Dp*NDT is also highly stable in a wide interval of pH values: it shows maximal stability within a pH range from 4.0 to 11.0 and maximal activity from 6.0 to 9.0 (Fig. 1D). It is worth to indicate that since the pK_1 value for Ura and Thy are around 9.5 [53,54] the observed pH-dependence should be only attributable to *Dp*NDT. *Ef*PDT is also active in a broad pH interval, ranging from 4 to 7, but in contrast to *Dp*NDT it shows maximum activity at pH 4 (Fig. 1D).

Optimal growth of *D. psychrophila* requires a concentration of NaCl around 10 g/L [38]. In this sense, *Dp*NDT activity decreases smoothly with increasing salt concentration up to 1 M NaCl, where 80% remaining activity is observed (Supplementary Fig. 1). Furthermore, its activity is almost insensitive to monovalent or divalent cations up to 50:1 (cation: enzyme) molar ratio, with the exception of $CuSO_4$ where a 70% decrease in activity is observed (Supplementary Fig. 2).

3.2. Structural characterization of DpNDT and EfPDT

With the aim to shed light on the structural basis of the high thermostability of *Dp*NDT we solved the crystal structures of both *Dp*NDT

and that of the closest structural, mesophilic homolog *Ef*PDT. High-quality diffraction crystals of *Ef*PDT diffracted up to 2.15 Å resolution and belonged to the cubic space group $F4_132$ with unit cell dimensions of $a = b = c = 219.9$ Å. The structure of *Ef*PDT was determined by Se-SAD phasing (*Ef*PDT has 2 Met out of 159 residues). The asymmetric unit of the crystal contained two identical polypeptide chains (r.m.s.d. of 0.24 Å for 156 Cα atoms) that associate as a dimer with the typical topological features of the basic catalytic unit of 2′-deoxyribosyltransferases [12]. With the exception of the side chains of residues 44-45 located at the β2-α2 connecting loop from chains A and B, and the C-terminal amino acid Ser159, all the residues are well defined in the $2mF_o$-DF_c electron density map. Conversely, *Dp*NDT crystals diffracted up to 2.4 Å resolution and belonged to the orthorhombic space group $P2_12_12_1$ with unit cell dimensions of $a = 55.17$, $b = 86.37$ and $c = 140.93$ Å. The crystal structure of *Dp*NDT was solved by molecular replacement using the atomic coordinates of *Ef*PDT. Four identical polypeptide chains appeared in the asymmetric unit that form a tetrameric assembly. The final model of *Dp*NDT included residues 10-51 and 57-153 (out of 151 amino acids) from chain A, residues 11-56 and 62-152 from chain B, residues 10-49 and 61-150 from chain C and residues 12-54 and 64-151 from chain D. As indicated above, the poor definition of the $2mF_o$-DF_c electron density map from the β2-α2 connecting loops (or the equivalent, structural ones) of NDTs (residues 44-45 in *Ef*PDT and 45-62 in *Dp*NDT) is a common observation in their structures, which is most probably results from the intrinsic flexibility of these regions [10]. One glycerol molecule, with equivalent positions and orientations, was identified within each active site, both in *Dp*NDT and *Ef*PDT.

Structural similarity searches and pairwise 3D alignment analyses carried out with FATCAT [55] reveal the conservation in *Ef*PDT and *Dp*NDT of the canonical fold of the 2′-deoxyribosyltransferases subunit [12]. In particular, their closest structural homologs are *Ll*NDT (PDB code:1F8X) [12], *Lh*PDT (PDB code: 1S2D) [13], *Bp*NDT (PDB code: 6EVS) [7], and the eukaryotic *Tb*PDT (PDB code: 2F62) [11] and *Lm*PDT (PDB code: 6QAI) [10] (Supplementary Table 3). Despite the low r.m.s.d. values (ranging from 2.44 to 3.15 Å for an average of 130 C_α atoms) a detailed inspection of the structures permits identifying specific systematic structural differences between *Dp*NDT and the group of the three bacterial homohexameric enzymes *Ll*NDT, *Lh*PDT and *Bp*NDT (herein defined for convenience as group 1), on the one hand, and between *Dp*NDT and the group composed of the dimeric enzymes *Tb*PDT and *Lm*PDT (group 2), on the other. *Ef*PDT can be classified within this latter group 2. In particular, members of the group 1 of enzymes mainly differ from *Dp*NDT in their C-terminal regions since they have a much shorter α5 helix and possess a long and irregular C-terminal stretch, following that helix, which is not present neither in *Dp*NDT nor in enzymes from group 2 (Fig. 2A). This is quite remarkable since these irregular segments are both structurally and functionally relevant: first, they stabilize the hexameric assembly of these bacterial enzymes by participating in interdimer contacts [10], and second, their C-terminal ends gain access into the substrate-binding pocket of the accompanying subunit from the same catalytic unit. Conversely, *Dp*NDT differs from members of group 2 of enzymes in that this set of proteins possess an inserted region between strand β4 and helix α4 that participates in intersubunit contacts that contribute to the stabilization of the dimeric assembly of *Tb*PDT and *Lm*PDT; *Ef*PDT, while displaying such an insertion (comprised by residues 101 to 129), it adopts a markedly different conformation compared to these latter two enzymes (Fig. 2B), that enables interactions with an

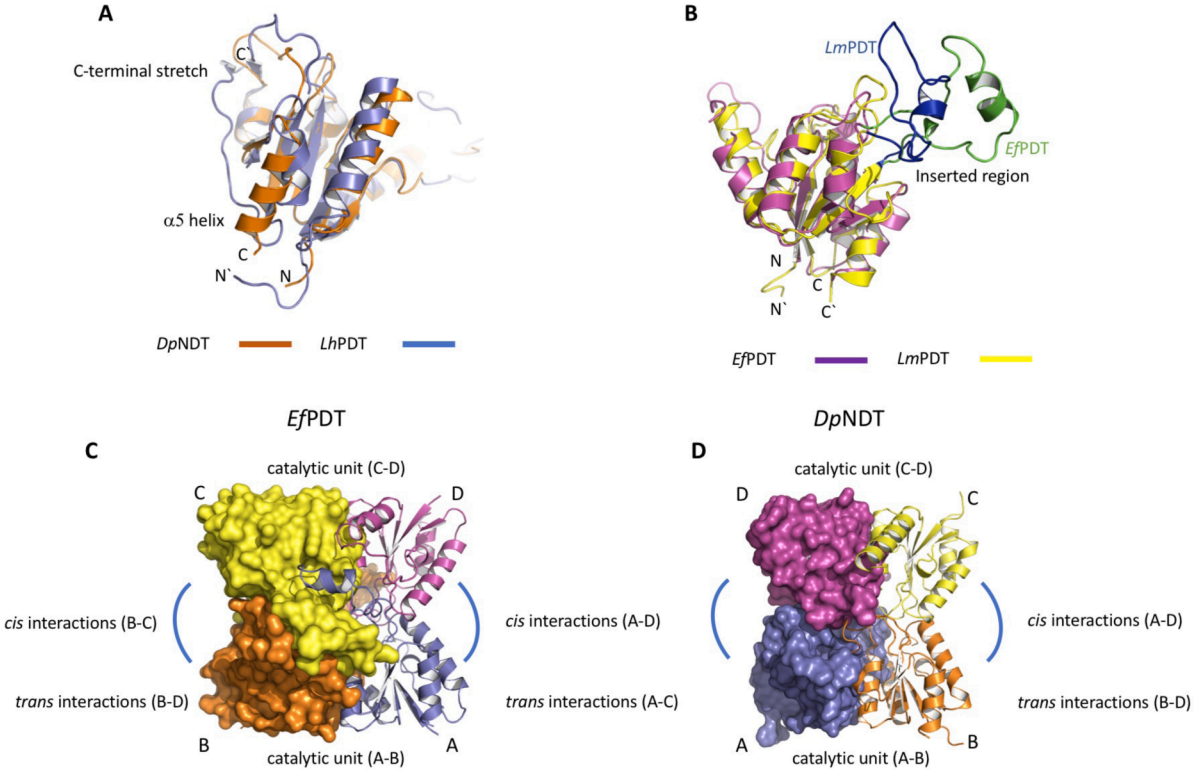


Fig. 2. Structural features differentiating *Dp*NDT from group 1 of enzymes and *Ef*PDT from other group 2 enzymes, and general topology and pattern of interactions between subunits in the tetramers of *Dp*NDT and *Ef*PDT. (a) The C-terminal region of the *Dp*NDT subunit presents a longer α5 helix compared to members of the group 1 of enzymes and lacks a long and irregular C-terminal stretch, following that helix, present in those homohexameric enzymes (see the text). (b) Structural differences in the inserted region of *Ef*PDT (in green) compared to other members of group 2 of enzymes (in this case, *Lm*PDT; inserted region in blue). (c) Tetrameric assembly of *Ef*PDT; two subunits (B and C) are shown as surface model and the other two as ribbon (A and D). (d) Tetrameric assembly of *Dp*NDT; two subunits (A and D) are shown as surface model and the other two as ribbon (B and C). In both tetramers, the two catalytic units are formed by subunits A-B and C—D, respectively. *Cis* and *trans* interactions between them are defined. To facilitate the identification of *cis* and *trans* interactions, and also the intersubunit interactions within the catalytic unit, we use the same color code for *Dp*NDT and *Ef*PDT in all the figures.

identical domain from a subunit of another catalytic unit in a *trans* mode (see below for its definition). Similar to the group 1 of enzymes, the C-terminal stretch from this inserted region forms part of the substrate-binding pocket of the accompanying subunit. The distinct structural features of *Dp*NDT and *Ef*PDT deduced from the above comparisons are consistent with their novel tetrameric assembly.

3.3. *EfPDT and DpNDT are tetramers*

Analysis of the *Ef*PDT crystal packing with PISA [35] identifies a tetramer as the highest order and highly stable assembly within the crystal (total buried area of 16,630 Å^2 with a total surface area of 23,630 Å^2, and a solvation free energy gain of -80.7 kcal/mol). The contacting interface between the catalytic units is very large; in particular, the interface between each pair of the crystallography related subunits (symmetry operator -x, -y, z) arranged in a *cis* mode (A-A′ or B-B′) is 1500 Å^2 and the one for subunits arranged in a *trans* mode (A-B′ or B-A′) is 1080 Å^2 (′ indicates a symmetry-related molecule). These values are comparable to the contacting interface between the subunits within the catalytic dimer of the asymmetric unit (1230 Å^2). For clarity, we will use the same nomenclature for subunits as with *Dp*NDT, and will defined molecule A′ as D, and molecule B′ as C (Fig. 2C).

PISA also identifies a *Dp*NDT tetramer as the highest-order stable assembly within the crystal packing (total buried area of 9890 Å^2 and a total surface area of 22,930 Å^2; solvation free energy gain of -85.7 kcal/mol). Hence, while both proteins have comparable total surface areas, *Dp*NDT has a much lower total buried (9900 Å^2 *vs* 16,648 Å^2), although the estimated solvation free energy gain upon *Dp*NDT tetramer formation is more favorable than for *Ef*PDT. The contacting interfaces between *Dp*NDT subunits from different catalytic units are 512 Å^2 (*cis* mode arrangement: A-D or B-C) and 312 Å^2 (*trans* mode arrangement: A-C or B-D), respectively (Fig. 2D). Despite sharing the same overall topology, the significant differences in the magnitude of their respective contacting interfaces foresee different stabilizing factors coming into play in both tetramers.

Tetramer formation is not driven by the high protein concentration within the crystal. Gel-filtration chromatography results obtained with *Ef*PDT are consistent with a tetramer in solution (Supplementary Fig. 3), and those obtained from the analysis of the hydrodynamic behaviour of *Dp*NDT by analytic ultracentrifugation agrees also with the presence of a tetramer. Sedimentation equilibrium results are consistent with the presence of a unique species in solution with an average molecular mass of 68 ± 4 kDa, (theoretical mass of the subunit: 16,747 Da) and sedimentation velocity studies indicates one hydrodynamic species in solution with an experimental sedimentation coefficient of 4.09 S (s20,w = 4.32).

The core, innermost region of the main contacting interface between catalytic units within *Ef*PDT and *Dp*NDT tetramers is formed by four connecting loops: β3-α4 in *Ef*PDT (residues 74-79) and β3-α3 in *Dp*NDT (residues 88-94). Local stabilizing interactions in this core region can be identified for each protein. In *Ef*PDT, the presence of Asp80 and Asp75 most probably stabilize the terminal macrodipole positively charges of helices α4 and α1 of a *cis* interacting subunit (Fig. 3A), respectively, and in *Dp*NDT the buried residues Asp94 and Asp95 would stabilize the macrodipole positive charge of helix α3 (Fig. 3B). A notable characteristic of *Ef*PDT is the abundance of cation-π interactions [56] between *cis*-

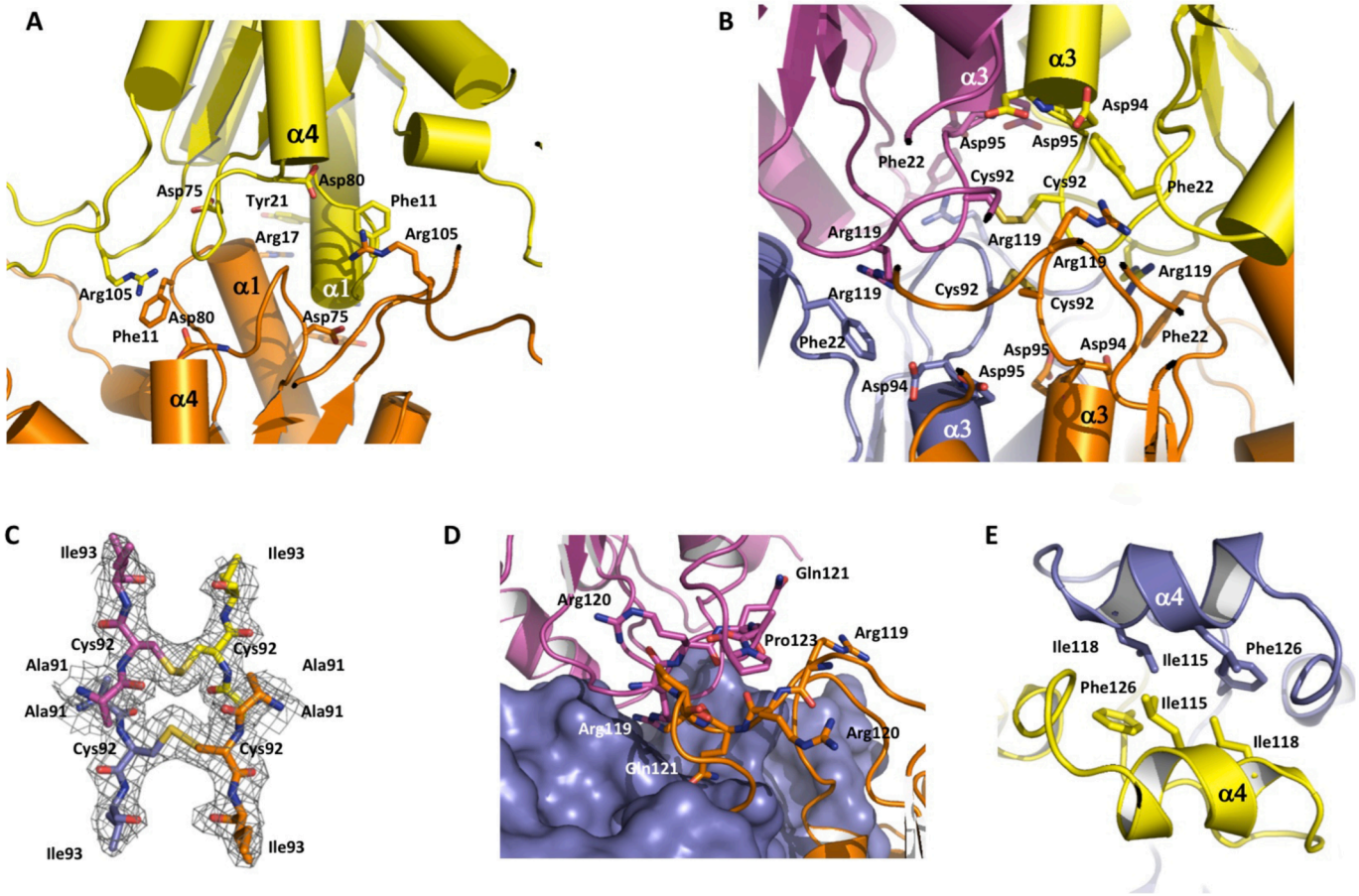


Fig. 3. Main intersubunit interactions within the *Ef*PDT and *Dp*NDT tetramers. Innermost core region of the main contacting interface between subunits of (a) *Ef*PDT and (b) *Dp*NDT, showing the principal *cis* interactions of the tetramers. (c) Close-up view of the two intersubunit disulfide bridges of *Dp*NDT showing the 2mFo-DFc electron density map (1σ level). *Trans* intersubunit contacts in (d) *Dp*NDT and in (e) *Ef*PDT. Same color code as in Fig. 2 has been used.

interacting subunits (Fig. 3A). Thus, helix α1 of one subunit interacts with the helix α1 of its *cis* counterpart through two cation-π interactions between Arg17 and Tyr21* and Tyr21 and Arg17*, respectively (for clarity, * denotes residues from a *cis* interacting subunit and # denotes residues from a *trans* interacting subunit), and similar interactions are identified between Phe11 and Arg105* and Phe11* and Arg105. In all these cases, the guanidinium moiety of the arginine side chains rests parallel to the aromatic ring, which is the preferred geometry for this type of interactions [57]. One cation-π interaction is identified in *Dp*NDT between *cis*-interacting subunits, in particular, between Phe22 from the β1-α1 loop and Arg119*.

Remarkably, the β3-α3 connecting loops of *Dp*NDT are stabilized by two disulfide bridges between Cys92 and Cys92• (• indicates residues from the other subunit of the same catalytic unit). As far as we know, this observation represents the first, intersubunit, covalent interaction described for 2′-deoxyribosyltransferases. Since these two disulfides are in close proximity (Fig. 3B), it is worth to remark that the 2mF_o-DF_c electron density map around them is perfectly defined and permits discarding either conformational heterogeneity or disulfide exchange (Fig. 3C). This consideration is important because it permits to ruled out the existence of covalent bonds between subunits from different catalytic dimers. It is expected that the presence of these bonds provided substantial global stability and also a well-defined geometry to the contacting interface.

As anticipated, *Ef*PDT and *Dp*NDT markedly differ in the magnitude of the contacting interface between their *trans* subunits (1080 *vs* 312 Å^2) and this is essentially due to the presence in *Ef*PDT of the inserted domain characteristic of group 2 enzymes. Thus, whereas in *Dp*NDT *trans* contacts are only observed between loops comprising residues Arg119-Pro123 and Arg119$^{\#}$-Pro123$^{\#}$ (Fig. 3D), in *Ef*PDT it is the large inserted domain (residues 101-129) between strand β4 and helix α4 (helix α5 in *Ef*PDT) the main structural element involved in *trans* interactions (Fig. 3E). The domain is composed of a small helix (helix α4 in *Ef*PDT) flanked by two irregular segments, the N-terminal one containing a helical turn (residues 103-107). The α4 helix of one subunit interacts (in a *trans* mode) with the same helix from an equivalent subunit, which pack together forming an antiparallel arrangement stabilized by a hydrophobic core made up of Leu115, Leu118, Phe126 side chains and the equivalent ones Leu115$^{\#}$, Leu118$^{\#}$, Phe126$^{\#}$. Interestingly, within the inserted region we have identified two residues that participate in *trans* and *cis* interactions (Supplementary Fig. 4): (i) Arg105, located at the N-terminal helical turn, and (ii) Glu123, situated at the C-terminal part of the domain. In the first case, the Arg105 side chain stacks on the aromatic ring of Phe11* (see the above-mentioned cation-π interactions) and also makes a weak hydrogen bond (3.3 Å) with the side-chain hydroxyl group of Tyr128$^{\#}$. These interactions are facilitated by a strong ionic interaction (2.7 Å distance) between Arg-104 and the carboxylate of Asp103. On the other hand, Glu123 interacts with Lys138$^{\#}$ from helix α5 (2.9 Å distance) and with Ser53*.

3.4. Cysteine residues in DpNDT

The sequence of *Dp*NDT reveals a relatively high content of cysteine residues (Cys40, Cys41, Cys92, Cys111, Cys132 and Cys134), which is an uncommon feature within the NDT family. Apart from the intersubunit disulfide bridge between Cys92 and Cys92•, the crystal structure of *Dp*NDT shows the formation of vicinal disulfides between Cys40 and Cys41, which is in itself a very rare structural feature [58] (Fig. 4). This vicinal disulfide is located in the α1-β2 connecting loop in close proximity to the large hydrophobic core of *Dp*NDT (see below). The conformational analysis of the vicinal disulfides shows that they exhibit a *trans* Tx conformation according to Richardson et al. [58] (Supplementary Table 4), with no evidence of conformational heterogeneity or *trans-cis* switching. The *trans* Tx conformation is more common than the *trans* Tz conformation, which in turn are more frequent than the two identified *cis* conformations (C+ and C-, respectively). Although some

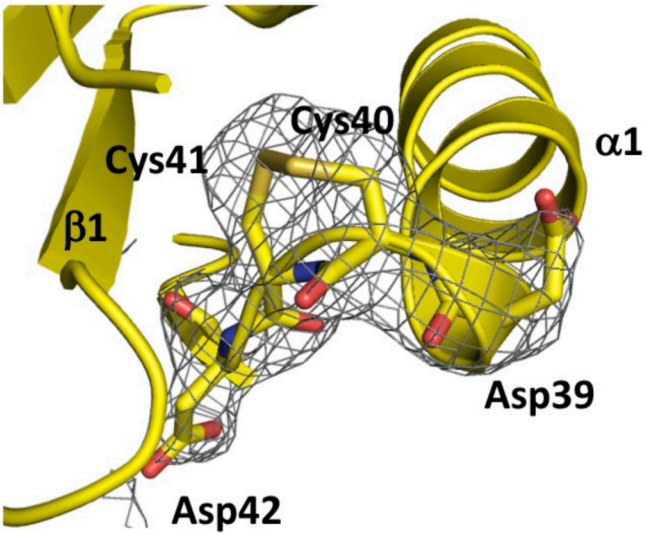


Fig. 4. Structure of the vicinal disulfide bridge found in the *Dp*NDT subunits. The 2mFo-DFc electron density map (1σ level) is shown in the region around the disulfide.

vicinal disulfides have been directly implicated in large-scale motions in proteins [58], most of them contribute to the formation of tightly packed regions, as it seems the case for *Dp*NDT.

The presence of intersubunit and vicinal disulfides is most probably a unique characteristic of *Dp*NDT as can be deduced from sequence similarity searches (Supplementary Fig. 5). This multiple sequence alignment (MSA) reveals the lack of cysteine residues equivalent to Cys40, Cys41 and Cys92 and also a high conservation of Cys111 and Cys134. Assuming a common topology for these *Dp*NDT close homologs, the observed distribution of cysteine residues in their sequences is not compatible with formation of intersubunit disulfide links. Additionally, this MSA also reveals that residues participating in intersubunit interactions within the *Dp*NDT tetramer (cation-π interactions), namely, Phe22 and Arg119*, and also Glu26, are strictly conserved in all the homologs, supporting the existence of such interactions in these proteins and therefore pointing to the existence of similar tetrameric assemblies. Further support for this idea comes from the fact that these latter interactions are not observed neither in hexameric (*Ll*NDT, *Lh*PDT and *Bp*NDT) nor dimeric (*Lm*PDT and *Tb*NDT) assemblies.

3.5. Active site

Catalytically important residues of *Ef*PDT and *Dp*NDT can be easily identified due to the conservation of the substrate-binding pocket of 2′-deoxyribosyltransferases [7,10]. These residues are Tyr5, Asp60, Asp80, Glu86, Asn130• and Tyr132• in *Ef*PDT and Tyr16, Asp74, Asp94, Glu100, Asn127• and Met129• for *Dp*NDT. Of note, *Ef*PDT lacks the methionine residue from the conserved motif NLM in 2′-deoxyribosyltransferases which is replaced by Tyr132. As a result of this, the immediate environment of their respective catalytic nucleophile (Glu86 in *Ef*PDT and Glu100 in *Dp*NDT) is markedly different, which may help explaining their different substrate specificity. In *Ef*PDT, we find two pairs of faced residues: Tyr5 with Tyr132• and Asp60 with Glu86 (Fig. 5A), respectively. The carboxylate of Glu86 forms a hydrogen bond with Tyr5 (2.5 Å distance) and also with a -OH group of a glycerol molecule (2.7 Å distance).

Interestingly, *Dp*NDT has an extra Met residue (Met78) within the active site, in a position where an Ile appears in all NDTs (Val in *Ef*NDT). This side chain packs against the aromatic ring of catalytic Tyr16 similarly to the aliphatic side chain of the Ile residue. Most probably, this highly conserved interaction with the catalytic tyrosine optimizes the orientation of the aromatic ring, facilitating H-bond formation with the

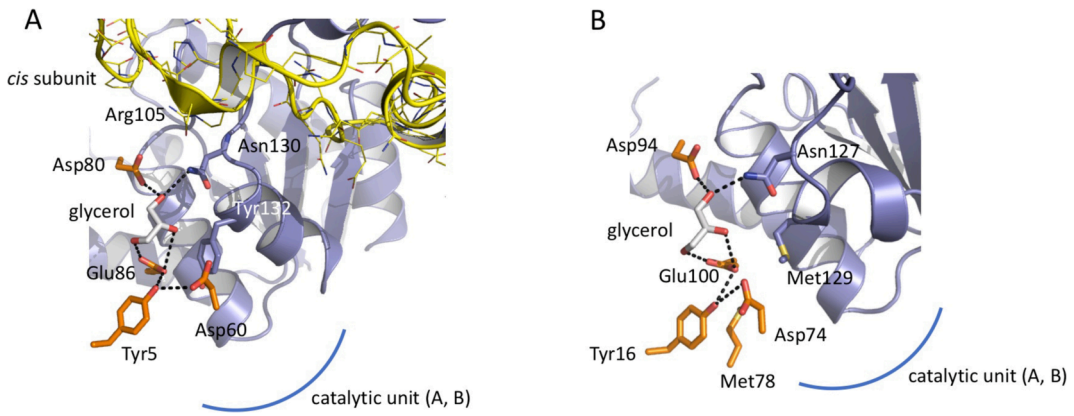


Fig. 5. Active sites of *Ef*PDT and *Dp*NTD. Catalytic residues of (a) *Ef*PDT and (b) *Dp*NDT are shown in *sticks* model. A glycerol molecule from the cryoprotectant solution occupies the same location in both proteins.

nucleophile side chain (Fig. 5B).

Finally, it is worth to mention that the presence of an inserted region in the enzymes belonging to the group 2 (Fig. 2B) results in a similar overall architecture of their substrate-binding pockets, which is different from those of group 1 and *Dp*NDT. Thus, in contrast to enzymes from group 1, the α5-α6 connecting loop of one subunit of *Lm*PDT or *Tb*NDT, or the N-terminal stretch of the inserted domain (residues 101-106) of *Ef*PDT, covers the substrate-binding pocket of its counterpart (Fig. 5A).

3.6. Structural basis of thermal stability of DpNDT

Our results show that *Dp*NDT is a highly thermostable psychrophilic enzyme with an apparent T_m of 58.5 °C, a value which is higher than the T_m of the tetrameric, mesophilic *Ef*PDT (55.5 °C). Estimation of the theoretical enthalpy change of protein unfolding (ΔH_{Tm}) from the changes in nonpolar and polar accessible surface area (ΔASA_{np} and ΔASA_p, respectively) carried out as previously reported for *Dp*IDH [43] agrees well with the above conclusion, providing a ΔH_{Tm} value for *Dp*NDT of 1270 kJ mol^{-1} and 1646 kJ mol^{-1} for *Ef*PDT. Nevertheless, comparison of these values is not as direct as in the case of *Dp*IDH with its mesophilic homolog, since *Ef*PDT possesses an additional structural element characteristic of enzymes from group 2 located between β4 strand and α4 helix, and therefore these numbers should be taken with caution. The presence of this extra region most probably explains the large difference in the values of buried area of assembly between both tetramers (9890 Å^2 for *Dp*NDT *versus* 16,648 Å^2 for *Ef*PDT), which in turn would affect to the estimated ΔH_{Tm} values. We have determined a large number of structural features for tetrameric (*Dp*NDT, *Ef*PDT), dimeric (*Lm*PDT, *Tb*NDT) and hexameric NDTs (*Ll*NDT, *Lh*PDT and *Bp*NDT) (Table 3) with the aim to reveal distinct structural features of *Dp*NDT supporting its high thermostability.

Table 3
Structural characteristics of 2′-deoxyribosyltransferases of known 3D structure.

	***Dp*NDT**	***Ef*PDT**	***Lm*PDT**	***Tb*NDT**	***Ll*NDT**	***Lh*PDT**	***Bp*NDT**
PDB entry	7O62	7M5H	6QAI	2F62	1F8X	1S2D	6EVS
No. aa/subunit[a] (nº aa/ assembly)	137 (548)	158 (632)	156 (312)	153 (306)	157 (942)	167 (1002)	142 (828)
Hydrophobic residues[b] (%)	55 (40.1)	71 (45.0)	76 (48.7)	68 (44.4)	63 (40.1)	72 (43.1)	75 (52.8)
Polar residues[c] (%)	42 (30.7)	49 (31.0)	43 (27.6)	43 (28.1)	51 (32.5)	49 (29.3)	39 (27.5)
Charged residues[d] (%)	40 (29.2)	38 (24.0)	37 (23.7)	42 (27.5)	43 (27.4)	46 (27.6)	28 (19.7)
Lys/Asp (%/%)	7.3/8.3	5.0/8.2	4.5/7.7	7.2/7.8	8.3/8.9	6.6/7.8	6.3/7.0
Cys residues (disulfide bonds)	6 (2)	0 (0)	2 (0)	3 (0)	0 (0)	2 (0)	0 (0)
ILV[e] (%)	24.6	27	19.9	18.9	20.4	13.8	15.4
No. H-bonds per residue in assembly[f]	2.20	3.20	1.79	2.04	2.21	2.11	1,99
pI[g]	4.56	4.51	4.81	5.23	4.65	4.93	4.70
No. SS[f,h] H-bonds per residue in assembly	0.48	0.43	0.23	0.30	0.40	0.47	0.31
No. SM[i] H-bonds per residue in assembly	0.43	0.47	0.32	0.52	0.50	0.49	0.39
No. MM[j] H-bonds per residue in assembly	1.29	2.30	1.24	1.22	1.31	1.15	1.29
No. ion pairs intrasubunit[f] 6 Å (4 Å)	19 (10)	13 (7)	7 (2)	13 (12)	19 (12)	15 (7)	11 (5)
No. 2-member networks 6 Å (4 Å)	10 (4)	3 (3)	2 (2)	3 (12)	4 (2)	6 (7)	3 (3)
No. 3-member networks 6 Å (4 Å)	0 (3)	2 (2)	1 (0)	2 (0)	3 (1)	1 (0)	2 (1)
No. 4-member networks 6 Å (4 Å)	0 (0)	2 (0)	1 (0)	2 (0)	0 (1)	0 (0)	1 (0)
No. >= 5-member networks 6 Å (4 Å)	1 (0)	0 (0)	0 (0)	0 (0)	2 (1)	1 (0)	0 (0)
No. ion pairs intersubunit[f] 6 Å (4 Å)	9 (5)	22 (4)	4 (1)	6 (4)	15 (15)	12 (6)	18 (3)
No. 2-member networks 6 Å (4 Å)	3 (5)	12 (4)	2 (2)	2 (0)	15 (15)	8 (6)	12 (3)
No. 3-member networks 6 Å (4 Å)	3 (0)	2 (0)	1 (0)	2 (2)	0 (0)	2 (0)	3 (0)
No. 4-member networks 6 Å (4 Å)	0 (0)	2 (0)	0 (0)	0 (0)	0 (0)	0 (0)	0 (0)
No. >=5-member networks 6 Å (4 Å)	0 (0)	0 (0)	0 (0)	0 (0)	0 (0)	0 (0)	0 (0)
T_m (ºC)	58.5	54.4	55	69	--	--	49
Accessible surface area[k] (*ASA*) of assembly (Å^2)	22,930	23,957	13,100	14,909	33,120	35,094	31,112
Buried area of assembly[l] (Å^2) (%)	9,890(43)	16,648(44)	4,585(40)	4,941(40)	17,265(49)	22,904(51)	15,809(48)
ΔASA_{np} (Å^2)	43,415	54,697	25,842	26,003	84,476	82,744	76,966
ΔASA_p (Å^2)	21,790	28,351	11,203	11,968	41,296	40,575	31,547
ΔC_pT (kJ K^{-1} mol^{-1})	57.98	67.13	36.43	35.90	114.03	111.54	110.49
ΔH_{60} (kJ mol^{-1})	1,328	2,385	559	653	2,440	2,406	1,425
ΔH_{Tm} (kJ mol^{-1})	1,270	1,646	377	976	--	--	209.6

3.6.1. Intersubunit disulfide

The contribution of the intersubunit disulfide bridge between Cys92 and Cys92• to the stability of *Dp*NDT has been analyzed by studying the thermal unfolding of His-*Dp*NDT and the single point mutant His-*Dp*NDTC92S, which lacks the disulfide. The thermal unfolding curves followed by far-UV CD, obtained under identical experimental conditions for *Ef*PDT and *Dp*NDT, revealed single, fully reversible transitions, with T_m values of (65.1 ± 0.9) °C for His-*Dp*NDT and (62.5 ± 0.2) °C for His-*Dp*NDTC92S, respectively (Supplementary Fig. 6). The difference in T_m values observed for *Dp*NDT and His-*Dp*NDT can be ascribed to the presence of the His-tag, as has been shown for other proteins (see [59] for a review). Assuming the same stabilizing effect of the His-tag is present in both His-*Dp*NDT and His-*Dp*NDTC92S (the amino acid change is buried in the oligomer structure), we can conclude that the presence of the intersubunit disulfide is a (modest) stabilizing structural element of *Dp*NDT. As expected, the higher thermal stability of the His-tagged enzymes has an impact on the temperature-dependence of their enzymatic activity. In particular, we observed that the remaining activities at 50 °C after 24 h. incubation were: 50% for *Dp*NDT (see Fig. 1B); 81% for His-*Dp*NDT and 70% for His-*Dp*NDT C92S, which parallels the thermal unfolding behaviour observed by CD spectroscopy.

3.6.2. ILV bundle

*Dp*NDT exhibits a hydrophobic core that is composed exclusively by aliphatic side chains of Ile, Leu and Val residues (ILV), which are contributed by helices α1 and α5, and strands β1 to β4. This type of cores, known as ILV bundles, have been identified before as regions of high stability that impede the penetration of water to their underlying main chain hydrogen bond networks, enhancing the protection against solvent exchange in NMR studies [60]. Analogous ILV bundles are also identified in both *Ef*PDT and *Ll*NDT, although in these cases an aromatic ring of a Phe residue can be observed (Phe6 in *Ef*PDT and Phe8 in *Ll*NDT) and therefore they cannot be rigorously defined as ILV bundles. Anyhow, the presence of these cores correlates well with the relative abundance of these amino acids in the amino acid composition of these enzymes, which amounts up to 24.6% in *Dp*NDT, 27% in *Ef*PDT and 20.4% in *Ll*NDT, respectively (Supplementary Table 5). Most probably, this aliphatic core contributes to the high stability of these proteins and in particular to *Dp*NDT which in addition presents vicinal disulfides in its close proximity, contributing further to the tight packing of this region as described in other cases [58].

3.6.3. Salt bridges

The analysis of the *Dp*NDT structure reveals 10 strong salt bridges within the subunit for a distance cutoff of 4 Å and 9 additional weaker ionic interactions (for a 6 Å cutoff), which are totally exposed to the solvent, excluding the bridge formed between Glu67 and Lys64. In this case, the Glu67 side chain is located in the buried face of helix α2 and Lys64 side chain is 20% buried. Remarkably, a large ionic network comprising 9 bridges (6 of them are strong) is identified (Fig. 6). In this network two positively charged residues (Lys27 and Arg31) would participate in networked salt-bridges with three other residues (Glu24, Asp54, Glu55, and Glu24, Glu28, Glu48, respectively), which is a statistically very infrequent feature as reported in a large-scale analysis of this type of interactions in proteins [61]. It is notable that a similar, extended ionic network has been described in *Dp*IDH [43]. Additionally, another 9 salt bridges (5 with a 4 Å cutoff) are observed involving intersubunit interactions: in particular, we identified two networked salt bridges between subunits from the same catalytic unit involving residues Lys64, Glu67 and Glu131• and two networked salt bridges between *cis* subunits involving residues Arg119, Glu26# and Asp94# which are totally buried within the contacting interface of the tetramer (Supplementary Fig. 7A). Finally, no salt bridges between *trans* subunits are observed in *Dp*NDT.

The tetramer of *Ef*PDT has seven strong, intrasubunit salt bridges, two of them buried in the protein structure (Asp103 with His127 and

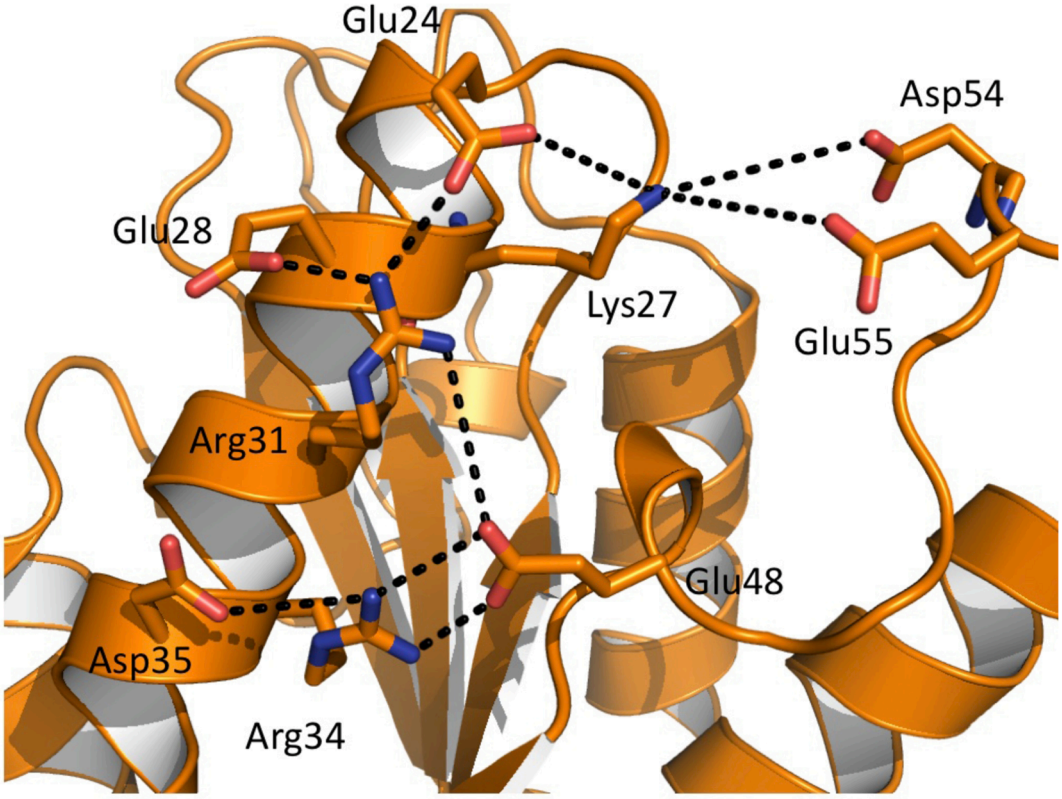


Fig. 6. Large ionic, 9-member network observed in *Dp*NTD. The presence of cationic residues (Lys27 and Arg31) interacting with three anionic partners is a highly unusual structural feature (see the text).

Asp103 with Arg105) and does not present a large ionic network similar to that observed in *Dp*NDT. Interestingly, the four strong, intersubunit salt bridges in *Ef*PDT, involving residues Glu123 and Lys138, are established between *trans* subunits (Supplementary Fig. 7B).

Although the presence in *Dp*NDT of a high number of salt bridges, both within subunits and between them in the oligomer, and the existence of a large ionic network, may have an impact on the high thermostability of *Dp*NDT, the specific contribution of such interactions to protein stability is not always straightforward and should require the specific analysis of each interaction [62]. In fact, both theoretical and experimental approaches "have arrived at the full range of possible conclusions regarding the contribution of salt bridges to protein stability - that salt bridges are generally destabilizing, that they have a negligible effect and that they are stabilizing to the overall protein structure" [61]. In this sense, the data shown in Table 3 agrees well with a positive correlation between total number of strong salt bridges (4 Å cutoff) and apparent T_m values for dimeric and tetrameric proteins, and also between the number of lysine residues and apparent T_m values, a correlation that has been supported recently in a cell-wide analysis of protein thermostability [63]. Likewise, the percentage of aspartic acid residues in this set of proteins, which is anticorrelated with protein thermostability [63], remains fairly constant.

3.7. Concluding remarks

As a whole, the structural features of *Dp*NDT that are exclusive for this enzyme when compared to the other members of this pleomorphic family and in particular to its mesophilic close homolog *Ef*PDT, are the existence of highly packed aliphatic core composed exclusively of Ile, Leu and Val residues (ILV bundle), combined with vicinal disulfides and also the presence of another disulfide bond between subunits of the catalytic unit. These structural features of the catalytic unit of *Dp*NDT (dimeric level) when integrated to a tetrameric assembly, with a specific balance between ΔASA_{np} and ΔASA_{p} upon unfolding, would be the main responsible of its high thermostability. In particular, the stabilizing effect of the intersubunit disulfide could be demonstrated with the single point mutant Cys92Ser.

Another interesting observation in this work is that despite the notable protein sequence divergence found in this set of proteins, their overall protein fold (subunit level) remains essentially identical as well as their catalytic function. The extreme case comes from *Ll*NDT and *Ef*PDT whose subunit structures superpose with a r.m.s.d. of 2.84 Å for 133 equivalent C_α atoms despite sharing 15% sequence identity (Supplementary Table 3). The high tolerance of a protein fold to sequence changes or robustness [64] is a strategy that highly expressed proteins within the cells have evolved for reducing protein misfolding [65], and precisely the level of protein expression within the cells has been recently shown to be correlated with global protein thermal stability [63]. We can speculate that thermostable enzymes from psychrophiles are highly expressed within the cells, which may compensate for their low activity in cold conditions. Hence, regulation of catalysis at low temperatures would transcend the protein level up to (at least) the subcellular level. In fact, the biological role of an enzyme should be understood as immersed in a multidimensional space with dimensions such as temperature, pH, salts and metals concentrations, molecular crowding, level of gene expression, global stability, protein lifetime and so on, and therefore it is expected that the specific molecular properties of enzymes resulted from the integration of all these dimensions. The projection of each dimension to the enzyme structure would most probably depend on the specific role of the enzyme within the specific cellular environment. Hence, a corollary of this is that any satisfactory explanation of enzymatic activity at low temperatures demands the analysis of the global stability of these psychrophilic enzymes in the presence of a cellular background, which has been shown to be critical for a rigorous determination of the global stability of mesophilic and thermophilic proteins [63].

Accession numbers

The atomic coordinates and structure factors have been deposited in the Protein Data Bank with the accession numbers 7M5H and 7O62 for *Ef*PDT and *Dp*NDT, respectively.

Author contributions

Conceptualized by J.F-L, P.A.K., I.D.L.M and J.M.M.; Experiments designed by J.F-L, M.A., A.J., B.P.N., I.D.L.M and J.M.M.; Experiments conducted by J.F-L, I.A., R.Y.W., Y.A., J.A.; Data analyzed by J.F-L, A.J., B.P.N., I.D.L.M and J.M.M.; Original draft-writing by J.M.M; Manuscript revision and editing by J.F-L., P.A.K., I.D.L.M. and J.M.M.

Declaration of competing interest

The authors declare that they have no conflict of interest.

Acknowledgements

J.M.M. thanks the ESRF (Grenoble, France) for provision of synchrotron-radiation facilities (ID29 beamline).

Funding

This work was supported by grants CTQ2009-11543 (IDLM), PID2020-117025RB-I00 (JF-L) and AGL2017-84614-C2-2-R (JMM) from the Spanish Ministry of Science and Innovation, S2009/PPQ-1752 (IDLM) from Comunidad Autónoma de Madrid and XSAN192006 (IDLM) from the Santander Foundation. This research was funded in part by National Institutes of Health grant (GM115586 to AJ). The use of SBC beamlines at the Advanced Photon Source is supported by the U.S. Department of Energy (DOE) Office of Science and operated for the DOE Office of Science by Argonne National Laboratory under Contract No. DE-AC02-06CH11357 (AJ).

Appendix A. Supplementary data

Supplementary data to this article can be found online at https://doi.org/10.1016/j.ijbiomac.2021.09.164.

References

[1] S.A. Short, S.R. Armstrong, S.E. Ealick, D.J.T. Porter, Active site amino acids that participate in the catalytic mechanism of nucleoside 2′-deoxyribosyltransferase, J. Biol. Chem. 271 (1996) 4978–4987, https://doi.org/10.1074/jbc.271.9.4978.

[2] A. Fresco-Taboada, I. De La Mata, M. Arroyo, J. Fernández-Lucas, New insights on nucleoside 2′-deoxyribosyltransferases: a versatile biocatalyst for one-pot one-step synthesis of nucleoside analogs, Appl. Microbiol. Biotechnol. 97 (2013) 3773–3785, https://doi.org/10.1007/s00253-013-4816-y.

[3] P.A. Kaminski, Functional cloning, heterologous expression, and purification of two different N-deoxyribosyltransferases from lactobacillus helveticus, J. Biol. Chem. 277 (2002) 14400–14407, https://doi.org/10.1074/jbc.M111995200.

[4] M.D. Erion, K. Takabayashi, H.B. Smith, J. Kessi, S. Wagner, S. Hönger, S. L. Shames, S.E. Ealick, Purine nucleoside phosphorylase. 1. Structure - function studies, Biochemistry 36 (1997) 11725–11734, https://doi.org/10.1021/bi961969w.

[5] R.F. Chawdhri, D.W. Hutchinson, A.O.L. Richards, Nucleoside deoxyribosyltransferase and inosine phosphorylase activity in lactic acid bacteria, Arch. Microbiol. 155 (1991) 409–411, https://doi.org/10.1007/BF00243463.

[6] K.A. Lawrence, M.W. Jewett, P.A. Rosa, F.C. Gherardini, Borrelia burgdorferi bb0426 encodes a 2′-deoxyribosyltransferase that plays a central role in purine salvage, Mol. Microbiol. 72 (2009) 1517–1529, https://doi.org/10.1111/j.1365-2958.2009.06740.x.

[7] A. Fresco-Taboada, J. Fernández-Lucas, C. Acebal, M. Arroyo, F. Ramón, I. De La Mata, J.M. Mancheño, 2′-deoxyribosyltransferase from bacillus psychrosaccharolyticus: a mesophilic-like biocatalyst for the synthesis of modified nucleosides from a psychrotolerant bacterium, Catalysts 8 (2018), https://doi.org/10.3390/catal8010008.

[8] J. Del Arco, P.A. Sánchez-Murcia, J.M. Mancheño, F. Gago, J. Fernández-Lucas, Characterization of an atypical, thermostable, organic solvent- and acid-tolerant 2′-deoxyribosyltransferase from chroococcidiopsis thermalis, Appl. Microbiol. Biotechnol. 102 (2018) 6947–6957.

[9] D.J. Steenkamp, T.J.F. Halbich, Substrate specificity of the purine-2'-deoxyribonucleosidase of crithidia luciliae, Biochem. J. 287 (1992) 125–129, https://doi.org/10.1042/bj2870125.
[10] N. Crespo, P.A. Sánchez-Murcia, F. Gago, J. Cejudo-Sanches, M.A. Galmes, J. Fernández-Lucas, J.M. Mancheño, 2′-deoxyribosyltransferase from leishmania mexicana, an efficient biocatalyst for one-pot, one-step synthesis of nucleosides from poorly soluble purine bases, Appl. Microbiol. Biotechnol. 101 (2017) 7187–7200, https://doi.org/10.1007/s00253-017-8450-y.
[11] J. Bosch, M.A. Robien, C. Mehlin, E. Boni, A. Riechers, F.S. Buckner, W.C. Van Voorhis, P.J. Myler, E.A. Worthey, G. DeTitta, J.R. Luft, A. Lauricella, S. Gulde, L. A. Anderson, O. Kalyuzhniy, H.M. Neely, J. Ross, T.N. Earnest, M. Soltis, L. Schoenfeld, F. Zucker, E.A. Merritt, E. Fan, C.L.M.J. Verlinde, W.G.J. Hol, Using fragment cocktail crystallography to assist inhibitor design of trypanosoma brucei nucleoside 2-deoxyribosyltransferase, J. Med. Chem. 49 (2006) 5939–5946, https://doi.org/10.1021/jm060429m.
[12] S.R. Armstrong, W.J. Cook, S.A. Short, S.E. Ealick, Crystal structures of nucleoside 2-deoxyribosyltransferase in native and ligand-bound forms reveal architecture of the active site, Structure 4 (1996) 97–107, https://doi.org/10.1016/S0969-2126(96)00013-5.
[13] R. Anand, P.A. Kaminski, S.E. Ealick, Structures of purine 2′-deoxyribosyltransferase, substrate complexes, and the ribosylated enzyme intermediate at 2.0 Å resolution, Biochemistry 43 (2004) 2384–2393, https://doi.org/10.1021/bi035723k.
[14] D. Georlette, V. Blaise, T. Collins, S. D'Amico, E. Gratia, A. Hoyoux, J.C. Marx, G. Sonan, G. Feller, C. Gerday, Some like it cold: biocatalysis at low temperatures, FEMS Microbiol. Rev. 28 (2004) 25–42, https://doi.org/10.1016/j.femsre.2003.07.003.
[15] W.H. Eschenfeldt, L. Stols, C.S. Millard, A. Joachimiak, M.I. Donnelly, A family of LIC vectors for high-throughput cloning and purification of proteins, in: S.A. Doyle (Ed.), High Throughput Protein Expr. Purif, Humana Press, 2009, pp. 105–115.
[16] M.M. Bradford, A rapid and sensitive method for the quantitation of microgram quantities of protein utilizing the principle of protein-dye binding, Anal. Biochem. 72 (1976) 248–254.
[17] L. Stols, C.S. Millard, I. Dementieva, M.I. Donnelly, Production of selenomethionine-labeled proteins in two-liter plastic bottles for structure determination, J. Struct. Funct. Genom. 5 (2004) 95–102, https://doi.org/10.1023/B:JSFG.0000029196.87615.6e.
[18] J. Fernández-Lucas, C. Acebal, J.V. Sinisterra, M. Arroyo, I. De La Mata, Lactobacillus reuteri 2'-deoxyribosyltransferase, a novel biocatalyst for tailoring of nucleosides, Appl. Environ. Microbiol. 76 (2010) 1462–1470, https://doi.org/10.1128/AEM.01685-09.
[19] J. Fernández-Lucas, A. Fresco-Taboada, C. Acebal, I. De La Mata, M. Arroyo, Enzymatic synthesis of nucleoside analogues using immobilized 2′-deoxyribosyltransferase from lactobacillus reuteri, Appl. Microbiol. Biotechnol. 91 (2011) 317–327, https://doi.org/10.1007/s00253-011-3221-7.
[20] P.H. Brown, P. Schuck, Macromolecular size-and-shape distributions by sedimentation velocity analytical ultracentrifugation, Biophys. J. 90 (2006) 4651–4661, https://doi.org/10.1529/biophysj.106.081372.
[21] T.M. Laue, B. Shah, T.M. Ridgeway, S.L. Pelletier, Computer aided interpretation of analytical sedimentation data for proteins, in: S.E. Harding, J.C. Horton, A.J. Rowe (Eds.), Anal. Ultracentrifugation Biochem. Polym. Sci, Royal Society of Chemistry, Cambridge, UK, 1992, pp. 90–125.
[22] A.P. Minton, Alternative strategies for the characterization of associations in multicomponent solutions via measurement of sedimentation equilibrium, Progr. Colloid Polym. Sci. 107 (1997) 11–19.
[23] S. Mazurenko, J. Stourac, A. Kunka, S. Nedeljkovi, D. Bednar, Z. Prokop, J. Damborsky, in: CalFitter : A Web Server for Analysis of Protein Thermal Denaturation Data 46, 2018, pp. 344–349, https://doi.org/10.1093/nar/gky358.
[24] W. Minor, M. Cymborowski, Z. Otwinowski, M. Chruszcz, HKL-3000: the integration of data reduction and structure solution - from diffraction images to an initial model in minutes, Acta Crystallogr. Sect. D Biol. Crystallogr. 62 (2006) 859–866, https://doi.org/10.1107/S0907444906019949.
[25] W. Kabsch, Acta Crystallogr. D Biol. Crystallogr. 66 (2010) 125–132, https://doi.org/10.1107/S0907444909047337.
[26] P.R. Evans, An introduction to data reduction: space-group determination, scaling and intensity statistics, Acta Crystallogr. Sect. D Biol. Crystallogr. 67 (2011) 282–292, https://doi.org/10.1107/S090744491003982X.
[27] T.R. Schneider, G.M. Sheldrick, Substructure solution with SHELXD, Acta Crystallogr. Sect. D Biol. Crystallogr. 58 (2002) 1772–1779, https://doi.org/10.1107/S0907444902011678.
[28] Z. Otwinowski, Daresbury Study Weekend Proceedings, SERC Daresbury Laboratory, Warrington, UK, 1991.
[29] K. Cowtan, DM: an automated procedure for phase improvement by density modification, Jt. CCP4 ESF-EACBM Newsl. Protein Crystallogr. 31 (1994) 34–38.
[30] P. Emsley, B. Lohkamp, W.G. Scott, K. Cowtan, Features and development of coot, Acta Crystallogr. Sect. D Biol. Crystallogr. 66 (2010) 486–501, https://doi.org/10.1107/S0907444910007493.
[31] A.J. McCoy, R.W. Grosse-Kunstleve, P.D. Adams, M.D. Winn, L.C. Storoni, R. J. Read, Phaser crystallographic software, J. Appl. Crystallogr. 40 (2007) 658–674, https://doi.org/10.1107/S0021889807021206.
[32] G.N. Murshudov, P. Skubák, A.A. Lebedev, N.S. Pannu, R.A. Steiner, R.A. Nicholls, M.D. Winn, F. Long, A.A. Vagin, REFMAC5 for the refinement of macromolecular crystal structures, Acta Crystallogr. Sect. D Biol. Crystallogr. 67 (2011) 355–367, https://doi.org/10.1107/S0907444911001314.
[33] P.V. Afonine, R.W. Grosse-Kunstleve, N. Echols, J.J. Headd, N.W. Moriarty, M. Mustyakimov, T.C. Terwilliger, A. Urzhumtsev, P.H. Zwart, P.D. Adams, Towards automated crystallographic structure refinement with phenix.refine, Acta Crystallogr. Sect. D Biol. Crystallogr. 68 (2012) 352–367, https://doi.org/10.1107/S0907444912001308.
[34] P.D. Adams, P.V. Afonine, G. Bunkoczi, V.B. Chen, I.W. Davis, N. Echols, J. J. Headd, L.W. Hung, G.J. Kapral, R.W. Grosse-Kunstleve, A.J. McCoy, N. W. Moriarty, R. Oeffner, R.J. Read, D.C. Richardson, J.S. Richardson, T. C. Terwilliger, P.H. Zwart, PHENIX: a comprehensive python-based system for macromolecular structure solution, Acta Crystallogr. Sect. D: Biol. Crystallogr. 66 (2010) 213–221, https://doi.org/10.1107/s0907444909052925.
[35] E. Krissinel, K. Henrick, Inference of macromolecular assemblies from crystalline state, J. Mol. Biol. 372 (2007) 774–797, https://doi.org/10.1016/j.jmb.2007.05.022.
[36] W.G. Touw, C. Baakman, J. Black, T.A.H. Te Beek, E. Krieger, R.P. Joosten, G. Vriend, A series of PDB-related databanks for everyday needs, Nucleic Acids Res. 43 (2015) D364–D368, https://doi.org/10.1093/nar/gku1028.
[37] W.L. DeLano, The PyMOL Molecular Graphics System, 2008.
[38] J. Kuever, F.A. Rainey, F. Widdle, Desulfotalea Knoblauch, Sahm and Jorgensen 1999, 1641VP, in: G.M. Garrity (Ed.), Bergey's Man. Syst. Bacteriol, 2005, pp. 997–999.
[39] T. Oikawa, T. Kazuoka, K. Soda, Paradoxical thermostable enzymes from psychrophile: molecular characterization and potentiality for biotechnological application, J. Mol. Catal. B Enzym. 23 (2003) 65–70, https://doi.org/10.1016/S1381-1177(03)00073-0.
[40] Y. Miyamoto, T. Masaki, S. Chohnan, Characterization of N-deoxyribosyltransferase from Lactococcus lactis subsp. lactis, Biochim. Biophys. Acta, Proteins Proteomics 1774 (2007) 1323–1330, https://doi.org/10.1016/j.bbapap.2007.08.008.
[41] P.A. Kaminski, P. Dacher, L. Dugué, S. Pochet, In vivo reshaping the catalytic site of nucleoside 2′- deoxyribosyltransferase for dideoxy- and didehydronucleosides via a single amino acid substitution, J. Biol. Chem. 283 (2008) 20053–20059, https://doi.org/10.1074/jbc.M802706200.
[42] E. Pérez, P.A. Sánchez-Murcia, J. Jordaan, M.D. Blanco, J.M. Mancheño, F. Gago, J. Fernández-Lucas, Enzymatic synthesis of therapeutic nucleosides using a highly versatile purine nucleoside 2'-DeoxyribosylTransferase from trypanosoma brucei, ChemCatChem 10 (2018) 4406–4416, https://doi.org/10.1002/cctc.201800775.
[43] A.E. Fedøy, N. Yang, A. Martinez, H.K.S. Leiros, I.H. Steen, Structural and functional properties of isocitrate dehydrogenase from the psychrophilic bacterium desulfotalea psychrophila reveal a cold-active enzyme with an unusual high thermal stability, J. Mol. Biol. 372 (2007) 130–149, https://doi.org/10.1016/j.jmb.2007.06.040.
[44] H.K.S. Leiros, A.E. Fedøy, I. Leiros, I.H. Steen, The complex structures of isocitrate dehydrogenase from clostridium thermocellum and desulfotalea psychrophila suggest a new active site locking mechanism, FEBS Open Bio. 2 (2012) 159–172, https://doi.org/10.1016/j.fob.2012.06.003.
[45] D. Odokonyero, A. Sakai, Y. Patskovsky, V.N. Malashkevich, A.A. Fedorov, J. B. Bonanno, E.V. Fedorov, R. Toro, R. Agarwal, C. Wang, N.D.S. Ozerova, W. S. Yew, J.M. Sauder, S. Swaminathan, S.K. Burley, S.C. Almo, M.E. Glasner, Loss of quaternary structure is associated with rapid sequence divergence in the OSBS family, Proc. Natl. Acad. Sci. U. S. A. 111 (2014) 8535–8540, https://doi.org/10.1073/pnas.1318703111.
[46] Á. Svingor, J. Kardos, I. Hajdú, A. Németh, P. Závodszky, A better enzyme to cope with cold: comparative flexibility studies on psychrotrophic, mesophilic, and thermophilic IPMDHS, J. Biol. Chem. 276 (2001) 28121–28125, https://doi.org/10.1074/jbc.M104432200.
[47] Y. Yamanaka, T. Kazuoka, M. Yoshida, K. Yamanaka, T. Oikawa, K. Soda, Thermostable aldehyde dehydrogenase from psychrophile, cytophaga sp. KUC-1: enzymological characteristics and functional properties, Biochem. Biophys. Res. Commun. 298 (2002) 632–637, https://doi.org/10.1016/S0006-291X(02)02523-8.
[48] T. Kazuoka, Y. Masuda, T. Oikawa, K. Soda, Thermostable aspartase from a marine psychrophile, cytophaga sp. KUC-1: molecular characterization and primary structure, J. Biochem. 133 (2003) 51–58, https://doi.org/10.1093/jb/mvg012.
[49] P.A. Fields, Review: protein function at thermal extremes: balancing stability and flexibility, Comp. Biochem. Physiol. A Mol. Integr. Physiol. 129 (2001) 417–431, https://doi.org/10.1016/S1095-6433(00)00359-7.
[50] G. Feller, Molecular adaptations to cold in psychrophilic enzymes, Cell. Mol. Life Sci. 60 (2003) 648–662, https://doi.org/10.1007/s00018-003-2155-3.
[51] K.S. Siddiqui, R. Cavicchioli, Cold-adapted enzymes, Annu. Rev. Biochem. 75 (2006) 403–433, https://doi.org/10.1146/annurev.biochem.75.103004.142723.
[52] A. Sadana, A deactivation model involving pH for immobilized and soluble enzymes, Biotechnol. Lett. 1 (1979) 465–470, https://doi.org/10.1007/BF01388428.
[53] S. Ganguly, K.K. Kundu, Protonation/deprotonation energetics of uracil, thymine, and cytosine in water from e.m.f./spectrophotometric measurements, Can. J. Chem. 72 (1994) 1120–1126, https://doi.org/10.1139/v94-143.
[54] V. Verdolino, R. Cammi, B.H. Munk, H.B. Schlegel, Calculation of pKa values of nucleobases and the guanine oxidation products guanidinohydantoin and spiroiminodihydantoin using density functional theory and a polarizable continuum model, J. Phys. Chem. B 112 (2008) 16860–16873, https://doi.org/10.1021/jp8068877.
[55] Z. Li, L. Jaroszewski, M. Iyer, M. Sedova, A. Godzik, FATCAT 2.0: towards a better understanding of the structural diversity of proteins, Nucleic Acids Res. 48 (2020) W60–W64, https://doi.org/10.1093/nar/gkaa443.
[56] J.P. Gallivan, D.A. Dougherty, Cation-π interactions in structural biology, Proc. Natl. Acad. Sci. U. S. A. 96 (1999) 9459–9464, https://doi.org/10.1073/pnas.96.17.9459.

[57] E.M. Duffy, W.L. Jorgensen, P.J. Kowalczyk, Do denaturants interact with aromatic hydrocarbons in water? J. Am. Chem. Soc. 115 (1993) 9271–9275, https://doi.org/10.1021/ja00073a050.
[58] J.S. Richardson, L.L. Videau, C.J. Williams, D.C. Richardson, Broad analysis of vicinal disulfides: occurrences, conformations with cis or with trans peptides, and functional roles including sugar binding, J. Mol. Biol. 429 (2017) 1321–1335, https://doi.org/10.1016/j.jmb.2017.03.017.
[59] W.T. Booth, C.R. Schlachter, S. Pote, N. Ussin, N.J. Mank, V. Klapper, L. R. Offermann, C. Tang, B.K. Hurlburt, M. Chruszcz, Impact of an N-terminal polyhistidine tag on protein thermal stability, ACS Omega 3 (2018) 760–768, https://doi.org/10.1021/acsomega.7b01598.
[60] S.V. Kathuria, Y.H. Chan, R.P. Nobrega, A. Özen, C.R. Matthews, Clusters of isoleucine, leucine, and valine side chains define cores of stability in high-energy states of globular proteins: sequence determinants of structure and stability, Protein Sci. 25 (2016) 662–675, https://doi.org/10.1002/pro.2860.
[61] J.N. Sarakatsannis, Y. Duan, Statistical characterization of salt bridges in proteins, Proteins Struct. Funct. Genet. 60 (2005) 732–739, https://doi.org/10.1002/prot.20549.
[62] C. Vetriani, D.L. Maeder, N. Tolliday, K.S.P. Yip, T.J. Stillman, K.L. Britton, D. W. Rice, H.H. Klump, F.T. Robb, Protein thermostability above 100 ° C : a key role for ionic interactions, Proc. Natl. Acad. Sci. U. S. A. 95 (1998) 12300–12305.
[63] P. Leuenberger, S. Ganscha, A. Kahraman, V. Cappelletti, P.J. Boersema, C. Von Mering, M. Claassen, P. Picotti, Cell-wide analysis of protein thermal unfolding reveals determinants of thermostability, Science (80-.) 355 (2017), https://doi.org/10.1126/science.aai7825.
[64] D.A. Drummond, J.D. Bloom, C. Adami, C.O. Wilke, F.H. Arnold, Why highly expressed proteins evolve slowly, Proc. Natl. Acad. Sci. U. S. A. 102 (2005) 14338–14343, https://doi.org/10.1073/pnas.0504070102.
[65] D.A. Drummond, C.O. Wilke, The evolutionary consequences of erroneous protein synthesis, Nat. Rev. Genet. 10 (2009) 715–724, https://doi.org/10.1038/nrg2662.